Soft Matter

RSC Publishing

PAPER

View Article Online
View Journal | View Issue

Cite this: *Soft Matter*, 2013, **9**, 11618

Expansion of charged colloids after centrifugation: formation and crystallisation of long-range repulsive glasses†

Marjolein N. van der Linden,* Djamel El Masri,‡ Marjolein Dijkstra and Alfons van Blaaderen*

Received 25th June 2013
Accepted 3rd October 2013

DOI: 10.1039/c3sm51752g

www.rsc.org/softmatter

We studied long-range repulsive glasses formed in suspensions of sterically stabilised charged colloidal poly(methyl methacrylate) particles ($\sigma = 2.23$ μm) with low polydispersity (4%) in the low-polar solvent cyclohexyl bromide ($\varepsilon_r = 7.92$). Particle interactions were described by a long-range repulsive Yukawa potential. Glasses were obtained upon compression of the suspensions by centrifugation from a body-centred-cubic crystalline structure at low initial volume fraction ($\eta \approx 0.02$) to a close-packed amorphous structure ($\eta \approx 0.64$). Subsequent expansion of the sediment in gravity resulted in long-range repulsive glassy structures with volume fractions $\eta = 0.16$–0.64. The presence of small clusters (mostly dumbbells; clustered fraction $f_{cl} \geq 0.12$) formed by centrifugation prevented the glasses from crystallising for several weeks, while the sediment was still expanding. We used confocal microscopy to obtain three-dimensional datasets of the system and quantitatively analysed the structure of the glasses. The structure of the glasses was found to be remarkably similar to that of hard-sphere glasses, for which experimental data were obtained by centrifugal compression of silica spheres with a hard potential, despite the much longer-range interaction potential. After more than ten weeks the clustered fraction decreased due to spontaneous dissociation of the clusters, and finally bulk crystallisation of the glasses was observed into face-centred-cubic crystals with a volume fraction of around 0.22.

1. Introduction

Colloidal systems are excellent model systems to study the behaviour of liquids, crystals, glasses and gels.[1] Experimental research on colloidal glasses has mainly been carried out using hard-sphere model systems.[2–10] Despite an increasing amount of research, the precise nature of the glass transition remains an unsolved problem.[11,12] Hard spheres exhibit a glass transition at a volume fraction $\eta \approx 0.56$–0.58, which was first found in systems of poly(methyl methacrylate) (PMMA) particles suspended in a decalin–carbon disulphide mixture,[8] and later investigated quantitatively by dynamic light scattering[2,3,9] and in 3D real-space studies.[5,6,10] In early studies agreement with mode-coupling theory (MCT) was found for colloidal hard spheres,[3] but more recent work by Brambilla *et al.* showed that the MCT description breaks down at high volume fractions.[9] These authors used dynamic light scattering experiments and Monte Carlo simulations to probe the dynamics in concentrated suspensions of colloidal hard spheres over a very large range (seven decades) of structural relaxation times τ_α. They found that the volume-fraction dependence of τ_α is well described by MCT up to the MCT glass transition volume fraction, but divergence of τ_α was found at a higher volume fraction than predicted by MCT.

The last decade has also seen an interesting development in the measurement of structure in glassy systems. Structural details of supercooled liquids and glasses, mostly in colloidal hard-sphere systems, were explored in experiments or simulations using methods based on bond order parameters,[13–16] Voronoi construction[17,18] and/or cluster-based analysis.[13,17] Novel reciprocal space methods have also been developed to elucidate the structure in colloidal and molecular glass-formers.[19,20]

Few experimental studies exist that focus on the glass transition in systems of charged colloidal spheres with a significant double layer compared to the particle size. In these systems the glass transition typically occurs at much lower volume fractions than for hard spheres. For example, in early work by Sirota *et al.*, X-ray scattering revealed a glass phase for $\eta > 0.20$ in a system of monodisperse charge-stabilised polystyrene colloidal spheres suspended in a methanol–water mixture.[21] Later, Härtl *et al.* found a glass transition at $\eta = 0.22$ in a suspension of colloids

Soft Condensed Matter, Debye Institute for Nanomaterials Science, Utrecht University, Princetonplein 5, 3584 CC Utrecht, The Netherlands. E-mail: M.N.vanderLinden@uu.nl; A.vanBlaaderen@uu.nl

† Electronic supplementary information (ESI) available: Movies corresponding to Fig. 4 and 10c and d; a movie corresponding to Section 3.2. See DOI: 10.1039/c3sm51752g

‡ Present address: EC2M, ESPCI-ParisTech, UMR Gulliver 7083, 75005 Paris, France.

made of polymerised perfluorobutylacrylate in a glycerol–water mixture.[22] Beck *et al.* applied static and dynamic light scattering to study a system of surface-functionalised silica colloids suspended in a glycerol–water mixture, for which a glass transition was found at $\eta = 0.18$.[23]

In recent studies the effect of soft or long-range repulsive interactions on the colloidal glass transition has been further explored. The Maret group investigated a 2D glass-forming binary mixture of super-paramagnetic particles with long-range dipolar interactions.[24,25] It should be noted that in 2D the glass transition can only be achieved when polydispersity is introduced. Mattsson *et al.* used dynamic light scattering to investigate a glass-forming system of microgel particles,[26] which have a soft, but short-range, interaction potential due to their deformable core. Klix *et al.* explored the effect of competing interactions on the glass transition in a system of PMMA particles with both long-range electrostatic repulsions and short-range depletion attractions.[27] By varying the interactions they found a gel state and two different glassy states. For the above-mentioned PMMA model system repulsive interactions are available that are sufficiently long-range to give rise to a body-centred-cubic crystalline phase at low volume fractions (<0.05); this can be achieved even for micrometre-sized colloids.[28–31] As far as we know glassy systems with such long-range repulsions have not yet been studied in real space.

This work is a quantitative 3D real-space study on the structure of long-range repulsive glasses formed in suspensions of sterically stabilised and charged colloidal particles with a double layer of the same size or larger than the particle size. More specifically, we employed a centrifugal compression technique that dates back to Hachisu and Takano, who used it to speed up the equilibration time to achieve a sedimentation equilibrium for charged polystyrene particles in water under normal gravity conditions.[32] First, the system was compressed to a metastable state by centrifugation and subsequently the sediment expanded towards an equilibrium state. These authors used charged particle systems with added salt to achieve thin double layers compared to the particle size, thus approximating a hard-sphere potential. The method was extended by Van Duijneveldt *et al.* to charged silica particles with a longer double layer that were dispersed in a refractive-index-matching mixture of toluene and ethanol.[33] Those authors centrifuged a dispersion of silica particles with a diameter of 700 nm into an amorphous glassy state (500*g*, 30 min; with *g* the gravitational acceleration) and had the system expand over several weeks. The original system crystallised into a face-centred-cubic (fcc) crystal at a volume fraction of 0.155. After a few hours of expansion, crystallisation was observed in the top of the sediment, while most of the sediment remained glassy. Even after several weeks, during which the top crystalline part grew to 2.3 mm in size (initial sediment length 1.7 cm), the bottom part remained amorphous. The crystal grown during the expansion was randomly stacked.

In the research presented in this paper we are extending these experiments on compressed particle systems to long-range repulsive systems in which even for micrometre-sized particles double layers can be still significantly larger than the particle size; body-centred-cubic (bcc) crystals are observed as the equilibrium phase if the next-nearest-neighbour interactions become sufficiently important.[28] The sterically stabilised PMMA particles that we used are similar to those of several other studies; cyclohexyl bromide is a common (co)solvent as this solvent almost index-matches the particles.[28–30,34–37] We intended to study the glass transition for long-range repulsive systems, which has hardly been investigated experimentally, and wanted to compare the long-range repulsive glasses with hard-sphere glasses also made by sedimentation in a similar way as presented before.[10] We expected the amorphous sediment to expand and crystallise or form re-entrant liquid phases, which were observed on several occasions before for this model system at intermediate volume fractions and low salt concentrations.[30,31] Such re-entrant melting behaviour was likely the result of a reduction of the particle charge with increasing volume fraction,[34,36] causing the particles to enter a regime of interparticle interaction parameters for which there is no crystal phase at intermediate volume fractions; this has been recently explored theoretically (up to a volume fraction of 0.30).[38] However, instead we observed that a significant fraction of the particles ($f_{cl} \geq 0.12$) formed clusters during compression by centrifugation. These clusters mainly consisted of two particles (so-called dumbbells), but nonetheless completely frustrated crystallisation. Only when, after 81 days of expansion, the repulsive interactions became stronger than the attractions and the particle clusters disappeared, did the system suddenly fully crystallise. Finally, it is relevant to mention that although it was found that a pairwise-additive interaction potential could describe the particle interactions at a range of volume fractions for parameters close to those studied here,[29] other studies strongly indicate that a pair interaction alone does not give a good description.[35,37,39,40]

This paper is organised as follows. In Section 2 we describe the model system, experimental procedure and data analysis, in Section 3 we discuss the results, and in Section 4 we present our conclusions.

2. Experimental methods

2.1. Model system

We used poly(methyl methacrylate) spheres (PMMA; density $d_{PMMA} = 1.19$ g cm^{-3}; dielectric constant $\varepsilon_r = 2.6$; refractive index $n_D^{25} = 1.492$),[41] sterically stabilised by a covalently bonded layer of a graft copolymer consisting of poly-(12-hydroxystearic acid) (PHSA) grafted onto a PMMA backbone.[42] The particles were synthesised by dispersion polymerisation[43,44] and labelled with the fluorescent dye 7-nitrobenzo-2-oxa-1,3-diazol (NBD), by covalent incorporation into PMMA.[43] The average diameter σ of the particles was 2.23 μm and the polydispersity 4%, as determined by scanning electron microscopy (SEM). To determine the average diameter and size polydispersity from the SEM images we measured ~100 particles using the program iTEM (Olympus Soft Imaging Solutions GmbH). The particles were suspended in cyclohexyl bromide (CHB; Acros Organics; density $d_{CHB} = 1.336$ g cm^{-3};[41] dielectric constant $\varepsilon_r = 7.92$;[45] refractive index $n_D^{25} = 1.4935$ (ref. 41 and

45)), which nearly matched the refractive index of the PMMA particles ($n_D^{25} = 1.492$). This solvent is known to decompose in time, a process which generates H^+ and Br^- ions (see ref. 31 and Chapter 2 of ref. 41). To reduce the ionic strength, we cleaned the solvent before use,[46] by bringing it into contact first with activated alumina (Al_2O_3; 58 Å, ~150 mesh, Sigma-Aldrich) and then with molecular sieves (4 Å, 10–18 mesh, Acros Organics). The conductivity of CHB after the cleaning steps was 5.2 pS cm^{-1} (Scientifica 627 conductivity meter). We measured the electrophoretic mobility of the particles at a volume fraction $\eta = 0.031$ (according to the method described in ref. 36) and from this we calculated an average charge number $Z = 609 \pm 22$ per particle. In Section 3.4 we will discuss the system parameters further.

The pair interaction in a system of charged colloidal particles is commonly described by a hard-core repulsive Yukawa (screened Coulomb) potential:[29,47–49]

$$\beta u_{ij}(r) = \begin{cases} \beta\varepsilon_{ij} \dfrac{\exp\left[-\kappa\left(r-\sigma_{ij}\right)\right]}{r/\sigma_{ij}} & r \geq \sigma_{ij} \\ \infty & r < \sigma_{ij} \end{cases}, \quad (1)$$

with $\sigma_{ij} = (\sigma_i + \sigma_j)/2$ and the contact value of the potential between two colloids i and j:

$$\beta\varepsilon_{ij} = \frac{Z_i Z_j}{(1+\kappa\sigma_i/2)(1+\kappa\sigma_j/2)} \frac{\lambda_B}{\sigma_{ij}}, \quad (2)$$

where r is the centre-to-centre distance between particles i and j, Z_i (Z_j) and σ_i (σ_j) are the charge number and diameter of colloid i (j), $\beta = 1/(k_B T)$, with k_B the Boltzmann constant, and T the absolute temperature. The Bjerrum length is given by

$$\lambda_B = \frac{e^2}{4\pi\varepsilon_r\varepsilon_0 k_B T}, \quad (3)$$

with e the elementary charge, ε_r the relative dielectric constant of the solvent and ε_0 the dielectric permittivity of vacuum. The Bjerrum length represents the distance at which the electrostatic interaction energy between two monovalent ions is equal to the thermal energy $k_B T$. The inverse Debye screening length is given by

$$\kappa = \sqrt{8\pi\lambda_B c_s}, \quad (4)$$

with c_s the concentration of the monovalent salt. The Debye screening length κ^{-1} indicates the thickness of the electrical double layer surrounding a colloidal particle and is a measure for the interaction range between two colloids. When the refractive index of the solvent closely matches that of the particles, as is the case in our experimental system, the Van der Waals interactions are much smaller than $k_B T$ and can be neglected.

For monodisperse systems, for which $\sigma_{ij} = \sigma$, the contact value of the potential between two colloids simplifies to

$$\beta\varepsilon = \frac{Z^2}{(1+\kappa\sigma/2)^2} \frac{\lambda_B}{\sigma}. \quad (5)$$

The electrostatic surface potential ψ_0 for an isolated particle can be approximated at low ψ_0 by[50]

$$\beta e\psi_0 = \frac{Z}{1+\kappa\sigma/2} \frac{2\lambda_B}{\sigma}. \quad (6)$$

Combining eqn (5) and (6) yields the relation between $\beta\varepsilon$ and ψ_0:

$$\beta\varepsilon = \frac{(\beta e\psi_0)^2}{4} \frac{\sigma}{\lambda_B}. \quad (7)$$

The hard-sphere system that we used for comparison consisted of 1.37 μm core–shell silica particles (determined by static light scattering (SLS); polydispersity ≈ 3%) with a 434 nm core labelled with the fluorescent dye fluorescein isothiocyanate (FITC),[10] suspended in a mixture of dimethyl sulphoxide (DMSO) and deionised water (8.2% water by weight); the refractive index closely matched that of the particles. We compared the radial distribution function $g(r)$ for experimentally obtained glassy structures to the $g(r)$ for computer-generated glassy structures; we found very good agreement, with an effective hard-sphere diameter only 3.6% larger than the diameter obtained from SLS. The double layer was thus thin compared to the particle diameter and we assumed the interactions could be described by a hard-sphere potential, similar to ref. 10.

2.2. Compression by centrifugation and confocal microscopy

We prepared PMMA suspensions with an initial volume fraction $\eta \approx 0.02$, which were transferred to a borosilicate glass capillary with inner dimensions 5 cm × 1.0 mm × 0.10 mm ($x \times y \times z$; VitroCom), mounted on a microscope glass slide. The suspension occupied approximately two-thirds of the capillary. The remaining part was filled with deionised water (milli-Q water, resistivity = 18.2 MΩ cm, Millipore), which acted as a sink for ions from the suspension, thus keeping the ionic strength low and the Debye screening length large. Both ends of the capillary were sealed with UV-curing optical adhesive (Norland no. 68).

We centrifuged the samples for 15–110 minutes at 15–107g (Eppendorf Centrifuge 5810), keeping the water phase on top. During centrifugation the particles were compressed on the water–CHB interface (PMMA has a lower density than CHB), where they formed a sediment; a schematic overview of the sample is shown in Fig. 1. The centrifugal field was directed along the long axis of the capillaries. After centrifugation the capillaries were stored vertically, with gravity pointing along the long axis.

We used confocal microscopy (Nikon C1 confocal microscope) with a 100× NA 1.4 oil immersion objective, in fluorescence mode with 488 nm excitation, to obtain three-dimensional stacks of images (typical stack: 256 × 256 × 129–184 pixels ($x \times y \times z$); the pixel size was in most cases 0.25 or 0.33 μm in xy and 0.27 or 0.39 μm in z; ~1.7 frames per second). Stacks were taken at several distances from the water–CHB interface, and at least 15 μm from the walls of the capillary to avoid wall-induced effects. During the measurements the capillaries were also kept in a vertical position, on a microscope frame tilted 90 degrees with respect to gravity.

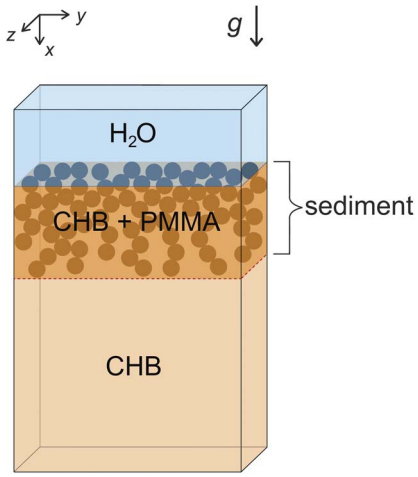

Fig. 1 Schematic overview of the sample after centrifugation (not drawn to scale). The glass capillary contained a water phase on top of a suspension of PMMA particles in CHB. The centrifugal field was pointing down (direction indicated by the arrow next to *g*), but the particles sedimented upwards (creamed) and were compressed on the water–CHB interface by the centrifugal field, where they formed a sediment. After centrifugation the capillaries were stored vertically, with gravity pointing down (direction indicated by the arrow next to *g*).

The hard-sphere silica system underwent a similar procedure. We constructed sample cells with inner dimensions ~2 cm × 6 mm × 150–180 μm, by glueing three strips of glass cut from a coverslip (thickness 130–160 μm, no. 1 coverslip, Menzel) in a U-shape onto a microscope glass slide using 2-component epoxy adhesive (Bison), and sticking a second coverslip on top. The glue was left to harden for at least 24 hours. The sample cells were filled from a Pasteur pipette with the suspension of silica in DMSO–water ($\eta \approx 0.10$) and centrifuged for at least 10 minutes at 9–2012*g* (Hettich Rotina 46 S centrifuge). After centrifugation, the open end was sealed with epoxy adhesive. We used a Leica TCS NT confocal microscope to image the samples (typical stack: 512 × 512 × 100 pixels ($x \times y \times z$); pixel size was 0.10 μm in *xy* and 0.20 μm in *z*; image stacks were taken at least 20 μm from the sample cell wall).

2.3. Data analysis

We obtained the positions of the particles using algorithms similar to those described in ref. 51 and 52. For subsequent data analysis we used all particles contained in a rectangular box with boundaries half a particle diameter from the edges of the image stack.

From the particle coordinates we calculated the radial distribution function $g(r)$, which describes the average positional order in the system. The radial distribution function gives the probability of finding a particle at a distance r from a given particle relative to the same probability in an uncorrelated configuration, or ideal gas, with the same number density. The quantity $4\pi r^2 \rho g(r)\mathrm{d}r$ is the number of particles found in a spherical shell of radius r and thickness dr around a given particle, where ρ is the average number density in the system.[53] We calculated the normalised probability distribution of pair distances for our system and corrected for the finite size of the box by dividing by the normalised probability distribution of pair distances which was calculated for an uncorrelated (ideal gas) configuration contained in a box of the same spatial dimensions (see also ref. 29).

The local bond-orientational order was examined as follows. For each particle i we defined a set of $2l + 1$ bond-orientational order parameters[54,55]

$$q_{lm}(i) = \frac{1}{N_\mathrm{b}(i)} \sum_{j=1}^{N_\mathrm{b}(i)} Y_{lm}\left(\theta_{ij}, \phi_{ij}\right), \tag{8}$$

where $N_\mathrm{b}(i)$ is the number of neighbours of particle i, θ_{ij} and ϕ_{ij} are the inclination and azimuth angles of the bond $\mathbf{r}_{ij} = \mathbf{r}_i - \mathbf{r}_j$ (where $\mathbf{r}_i$ ($\mathbf{r}_j$) denotes the position of particle i (j)) connecting the centres of particle i and its neighbour j, and $Y_{lm}(\theta_{ij}, \phi_{ij})$ are the spherical harmonics (with $m = -l, -l + 1, \ldots, l - 1, l$). The sum runs over all neighbours of particle i. The neighbours of particle i were defined as all particles within a certain cut-off distance r_c from particle i.

We used these sets of bond-orientational order parameters to calculate three different rotational invariants: $\hat{w}_l$, $\bar{q}_l$ and $\bar{w}_l$, as described below.

The local bond-orientational order parameter $\hat{w}_l$ was calculated in the following way:[54]

$$\hat{w}_l(i) = \frac{\sum_{m_1+m_2+m_3=0} \begin{pmatrix} l & l & l \\ m_1 & m_2 & m_3 \end{pmatrix} q_{lm_1}(i) q_{lm_2}(i) q_{lm_3}(i)}{\left(\sum_{m=-l}^{l} |q_{lm}(i)|^2 \right)^{3/2}}, \tag{9}$$

where $q_{lm}(i)$ is defined in eqn (8) and the coefficient in the numerator is a Wigner 3*j* symbol;[56] the integers m_1, m_2 and m_3 run from $-l$ to $+ l$, provided $m_1 + m_2 + m_3 = 0$. $\hat{w}_l$ is one of the order parameters defined by Steinhardt *et al.* (denoted by them as $\hat{W}_l$).[54] For hard-sphere glasses, the distribution of $\hat{w}_6$ was reported in ref. 10 (denoted in ref. 10 as W_6), enabling us to compare the structure of our long-range repulsive glasses to that of hard-sphere glasses.

Due to thermal fluctuations, the distributions of the Steinhardt order parameters can be rather broad, making it difficult to determine the type of local environment for each individual particle. Instead, we followed the method of Lechner and Dellago.[55] They averaged the sets of bond-orientational order parameters from eqn (8) over the central particle and its nearest neighbours. The distributions of these averaged order parameters are much narrower than those of the Steinhardt order parameters, and very suitable to distinguish between disordered and crystalline particle environments, as well as, in the latter case, to determine the type of crystalline environment.

So, we averaged each of the members of the set from eqn (8) over the central particle and its neighbours, to obtain for each particle i a set of *averaged* bond-orientational order parameters

$$\bar{q}_{lm}(i) = \frac{1}{N_\mathrm{b}(i) + 1} \sum_{j=0}^{N_\mathrm{b}(i)} q_{lm}(j), \tag{10}$$

where the sum runs over all neighbours of particle i plus particle i itself. From these sets of averaged bond-orientational

order parameters, we obtained the averaged local bond-orientational order parameters[55]

$$\bar{q}_l(i) = \sqrt{\frac{4\pi}{2l+1}\sum_{m=-l}^{l}|\bar{q}_{lm}(i)|^2} \quad (11)$$

and

$$\bar{w}_l(i) = \frac{\sum_{m_1+m_2+m_3=0}\begin{pmatrix} l & l & l \\ m_1 & m_2 & m_3 \end{pmatrix}\bar{q}_{lm_1}(i)\bar{q}_{lm_2}(i)\bar{q}_{lm_3}(i)}{\left(\sum_{m=-l}^{l}|\bar{q}_{lm}(i)|^2\right)^{3/2}}, \quad (12)$$

where $\bar{q}_{lm}(i)$ is defined in eqn (10) and the coefficient and sum in the numerator are the same as in eqn (9).

Finally, we looked at the fraction of crystalline particles in the system. Crystalline particles were identified by calculating the correlation between the sets of bond-orientational order parameters for each pair of neighbouring particles, given by

$$c_l(ij) = \frac{\sum_{m=-l}^{l} q_{lm}(i)q^*_{lm}(j)}{\left(\sum_{m=-l}^{l}|q_{lm}(i)|^2\right)^{1/2}\left(\sum_{m=-l}^{l}|q_{lm}(j)|^2\right)^{1/2}}, \quad (13)$$

where $q^*_{lm}(j)$ is the complex conjugate of $q_{lm}(j)$, and $q_{lm}(i)$ and $q_{lm}(j)$ are defined in eqn (8). A neighbour j to particle i was defined as a connected neighbour if $c_l(ij)$ exceeded a threshold value c_c. Particles with more than a certain number n_c of connected neighbours were defined as crystalline particles.[57] The crystalline fraction is then $f_X = N_X/N$, with N_X the number of crystalline particles and N the total number of particles in a certain volume of the sample. For our analysis we chose $l = 6$, $r_c = 1.5\rho^{-1/3}$ (with $\rho = N/V$ the number density of the particles, and $\rho^{-1/3}$ the characteristic interparticle distance), $c_c = 0.6$ and $n_c = 8$.

Instead of using a cut-off distance, which is always arbitrary, to define the nearest neighbours of a particle, it is possible to use the Voronoi construction to define neighbours. To this end, the Voronoi cell for each particle is calculated, containing all points in space that are closer to that particle than to any other particle. Particles that share a Voronoi face can now be defined as nearest neighbours. This method was used in ref. 10 for hard-sphere glasses to calculate the $\hat{w}_6$ distribution (as mentioned above). The distribution of the number of faces per Voronoi cell $P(n_n)$ (which is the same as the number of neighbours per particle) and the distribution of number of edges per Voronoi face $P(n_e)$ were also calculated. We employed the Voronoi construction to define neighbours for some of our datasets in order to compare with ref. 10.

The Steinhardt bond order parameters (in our case, $\hat{w}_l$, defined in eqn (9)) depend on the arrangement of the nearest neighbours of the central particle, *i.e.* the first-neighbour-shell particles. In our analysis, we calculated $\hat{w}_l$ for particles that were at least a distance r_c from the box boundaries, thus ensuring that we did not miss out some of the neighbours. When we used the Voronoi construction to define neighbours, we included only the $\hat{w}_l$ values of particles that were fully surrounded by neighbours, *i.e.* particles that did not share a Voronoi face with the box boundary. The averaged bond order parameters ($\bar{q}_l$, $\bar{w}_l$), as well as the crystallinity calculated through the bond order correlation method, depend also on the position of the second-neighbour-shell particles. Therefore, $\bar{q}_l$, $\bar{w}_l$ and the crystallinity were only calculated for particles that were at least a distance $2r_c$ from the box boundaries. In the Voronoi case, we included only the values of particles whose neighbours were fully surrounded by neighbours.

We used a distance criterion to identify particles that were part of a cluster: particles that had at least one neighbour at a distance $r < r_{cl}$ were defined as clustered particles. The *clustered* fraction is then $f_{cl} = N_{cl}/N$, with N_{cl} the number of clustered particles, *i.e.* particles part of a cluster, and N the total number of particles in a certain volume of the sample. We chose r_{cl} between the main peak of the $g(r)$ and the small peak at smaller distance close to the main peak, which resulted in $r_{cl} = 1.1\sigma$. With increasing volume fraction the probability to find two non-clustered particles separated by a distance $r < r_{cl}$ increases. For denser systems, it was therefore not possible to find the clustered fraction *via* this distance analysis procedure, and we did not plot f_{cl} for configurations with $\eta > 0.30$, a value chosen somewhat arbitrarily.

3. Results and discussion

We imaged the samples with confocal microscopy, obtaining ~20 three-dimensional datasets along the entire height of the sediment (typical spacing between datasets was 100 μm). We centrifuged samples at different speeds (15–107*g*) and followed them a few days to a week. We found no qualitative dependence of the resulting structures on the centrifugation speed. Two samples (centrifuged at 15*g* for 110 minutes and at 42*g* for 40 minutes) were followed during a much longer time period (2–3 months). Both samples had not fully sedimented after centrifugation was stopped and showed similar behaviour in time, including particle clustering. Below, we describe the behaviour of one of these samples (centrifuged at 15*g*), which we analysed in detail.

Section 3.1 gives an overview of the expansion and contraction of the sediment in time and the resulting volume fraction profiles of the sediment. In Section 3.2 we describe the formation and crystallisation of long-range repulsive glassy structures and show the correlation between the presence of glassy structures and clustered particles. In Section 3.3 the structural analysis of the glassy parts is described in detail and the structure is compared to that of hard-sphere glasses. In Section 3.4 we report on the structural analysis of the crystalline parts and the crystal symmetries that were identified. Finally, in Section 3.5, we describe additional experiments we performed to investigate the mechanism of clustering and declustering and we discuss a possible origin of the attractions responsible for cluster formation.

3.1. Expansion and contraction of the sediment

The sample was imaged directly after centrifugation ($t = 0$ days after compression by centrifugation) and subsequently after 1,

2, 4, 7, 14, 21, 35, 49, 64 and 81 days. We calculated the volume fraction η in each of the datasets from the number of particles N found by the tracking routine, the average particle diameter σ and the volume of the box V in which the particles were contained, through $\eta = N\pi\sigma^3/(6V)$. The left part of Fig. 2 shows the volume fraction profiles (volume fraction η *versus* distance x from the water–CHB interface) for different times t. We show the results of six different measurement days.

A centrifugal field or (after centrifugation) gravity caused the particles to migrate towards the water–CHB interface, which was located at $x = 0$ mm. Directly after centrifugation ($t = 0$ days), the particles that were furthest from the interface were still moving towards the interface, because, as was mentioned above, the sample had not been fully compressed during centrifugation; this caused the total height of the sediment to decrease. Here, the total height of the sediment is the distance from the interface beyond which virtually no particles can be found. In Fig. 2 the total height of the sediment at $t = 0$ days is beyond the scale of the graph. After 2 days the total height reached a value slightly less than 2 mm (Fig. 2, left, second panel from top), after which it started to increase. Meanwhile, the dense part of the sediment, close to the interface, which had been compressed by the centrifugal field, started to expand and particles migrated away from the interface. These particles had been forced into a close-packed and amorphous configuration by the centrifugal field. Without the presence of this field, the dense part of the sediment expanded due to the repulsive interactions between the charged particles. This effect caused the total height of the sediment to reach a maximum value at $t =$ 7 days. For $t = 7$–64 days, the total height slowly decreased again. Presumably, this was due to an increasing concentration of background ions and thus decreasing Debye screening length, most likely caused by the slow decomposition of the solvent CHB, a process which generates ions (H^+ and Br^-, as mentioned above). Apparently, the uptake of ions by the water phase was not sufficient to keep the ionic strength constant. See below (Section 3.4) for estimates of the decrease of $(\kappa\sigma)^{-1}$ as a result of the increase in ionic strength, which was initially low enough to allow parts of the system to crystallise with bcc symmetry.

This sequence of events is consistent with the values for the maximum volume fraction found in the sediment. The maximum volume fraction was $\eta = 0.64$ at $t = 0$ days, and reached a temporary minimum at $t = 14$ days, $\eta = 0.24$ (not shown), expansion of the dense part of the sediment being the dominant effect. After that it increased slowly and

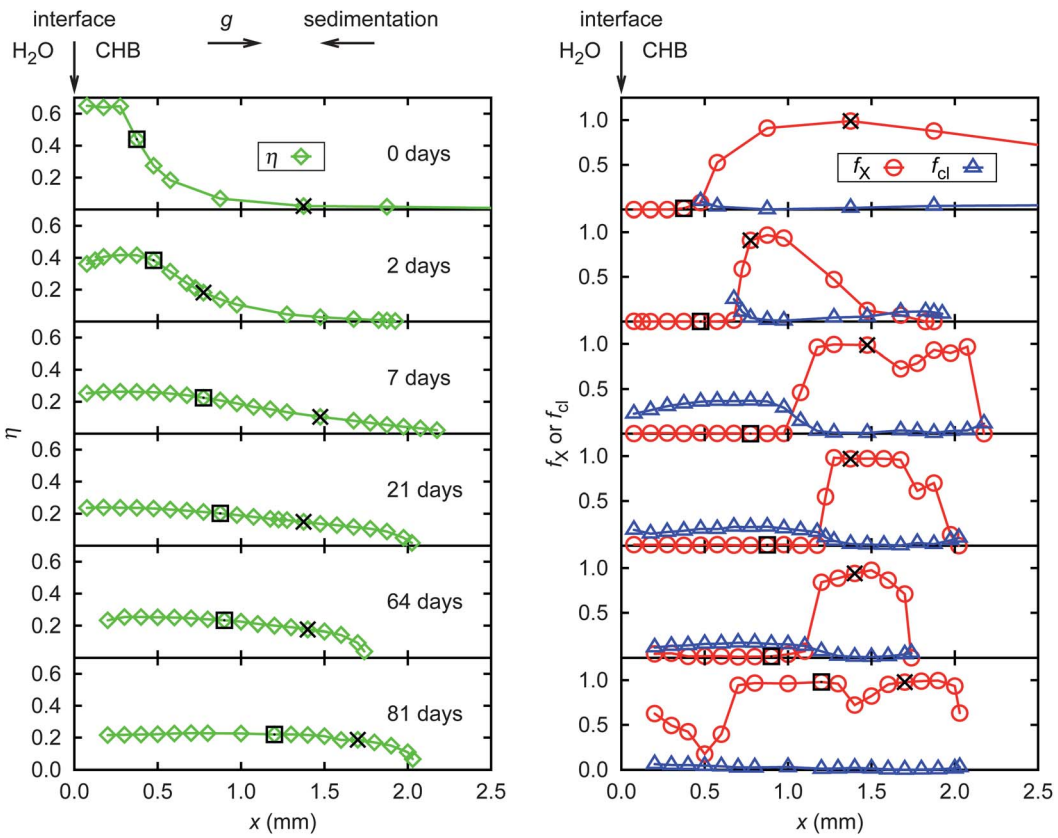

Fig. 2 Volume fraction η (left), and crystalline fraction f_X and clustered fraction f_{cl} (right) plotted *versus* the distance from the water–CHB interface x for different waiting times ($t = 0$–81 days). Black squares and black crosses indicate respectively an initially (at $t = 0$ days) glassy and initially crystalline spot in the sediment; the position of these spots changed in time due to expansion and contraction of the sediment. The configurations correspond to data points in Fig. 3b (squares) and Fig. 3c (crosses). At the top of the figure we indicate the position of the water–CHB interface (at $x = 0$ mm), the direction of gravity (g) and the direction of sedimentation of the particles.

continuously to $\eta = 0.25$ at $t = 64$, presumably due to a decrease in screening length. In time the volume fraction profile flattened out to an almost horizontal line at $t = 81$ days (Fig. 2, left, bottom panel).

At $t = 81$ days we found an increased total height and a decreased maximum volume fraction ($\eta = 0.23$). On this measurement day we observed large particle-free droplets (~5 to 40 μm, possibly containing water or air) in the CHB phase close to the water–CHB interface. Since the droplets contained no particles, they pushed the particles away from the interface, increasing the height of the sediment. The decreased volume fraction suggests that the Debye screening length also increased.

3.2. Formation and crystallisation of glassy structures

For each dataset, we calculated the crystalline fraction f_X and the clustered fraction f_{cl} (the fraction of particles that was part of a cluster), using the methods described in Section 2.3. The right part of Fig. 2 shows the crystalline fraction f_X and clustered fraction f_{cl} *versus* distance x from the water–CHB interface for different times after centrifugation was stopped. In addition, Fig. 3a shows the number of particles, number of crystalline particles and number of clustered particles in the entire sediment, obtained by integrating the volume fraction profiles in Fig. 2 over the volume of the suspension in the capillary and dividing by the volume of a single particle $v = \pi\sigma^3/6$.

We expect the number of particles in the system to stay constant. This was indeed the case for $t = 4$–64 days, as indicated by the dashed black line through the green diamonds in Fig. 3a. For $t < 4$ days not all particles were correctly identified by the tracking routine due to the high densities of the system close to the water–CHB interface. For $t = 81$ days, the number of particles was overestimated due to the presence of particle-free droplets of water in the CHB phase, as mentioned above.

Before centrifugation, we checked the sample ($\eta \approx 0.02$), and found that it was fully crystalline with the crystal phase being bcc. We discuss the symmetries of the crystalline parts in more detail in a separate section below (Section 3.4). After centrifugation, we found subsequently (moving through the sediment away from the interface) a glassy part adjacent to the interface (with $f_X < 0.05$), a crystalline part and a fluid part (Fig. 2, right). The system stayed like this until $t = 64$ days. During this time period no extensive crystallisation took place, as we can see from the fact that the total number of crystalline particles hardly changed (Fig. 3a), comprising ~25% of the total number of particles in the sediment (indicated by the dashed black line through the red circles in Fig. 3a). The number of clustered particles during the same period decreased, but from $t = 21$ days only very slowly, reaching a kind of plateau with a value corresponding to ~13% of the total number of particles (indicated by the dashed black line through the blue triangles in Fig. 3a). At $t = 81$ days we found that the number of clustered particles (~3% of the particles) was much lower than before, while a significant part of the sample had crystallised (~88% of the particles were crystalline) (these numbers were calculated using the total number of particles in the sample indicated by the dashed black line in Fig. 3a).

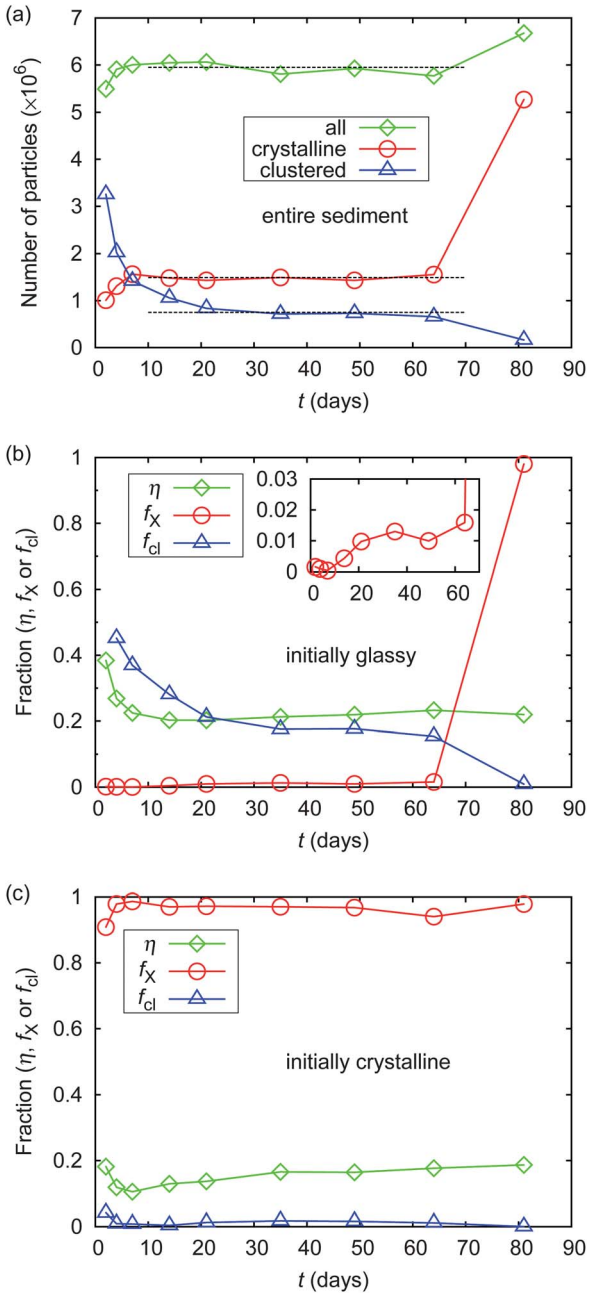

Fig. 3 (a) Number of particles, number of crystalline particles and number of clustered particles in the entire sediment as a function of waiting time t. (b) Volume fraction η, crystalline fraction f_X and clustered fraction f_{cl} as a function of waiting time t for an initially (at $t = 0$ days) glassy spot in the sediment (black squares in Fig. 2). The inset shows f_X at a different scale. (c) The same, but for an initially crystalline spot (black crosses in Fig. 2).

From the right part of Fig. 2 we see that the clusters were not evenly distributed across the sediment. In general, f_{cl} was high in places where f_X is low, and *vice versa*, *i.e.* the glassy part contained more clusters than the crystalline part. As mentioned above, the clustered fraction f_{cl} is not plotted for the denser part of the sediment ($\eta > 0.30$) at $t = 0$ and 2 days, since we could not

use a distance criterion to correctly identify clusters in denser systems. The slight increase in f_{cl} on the low-density side of the sediment is not real, but due to particles that were erroneously found twice by the tracking routine, and therefore can be ignored.

To quantify the difference between a typical glassy and typical crystalline configuration, we depicted in Fig. 3b and c in more detail the behaviour of η, f_X and f_{cl} in time for two particular spots in the sample: one located in the part of the system that was initially glassy (Fig. 3b and black squares in Fig. 2), the other from the part of the system that was initially crystalline (Fig. 3c and black crosses in Fig. 2). From the integrated volume fraction profiles we were able to locate approximately the same spot in the sample for each measurement day. The spots were located by counting particles starting from the low-density side of the sediment: on each measurement day approximately the same number of particles could be found on the low-density side of the indicated spot. The clustered fraction in the initially glassy configuration decreased from $f_{cl} = 0.45$ at $t = 4$ days to $f_{cl} = 0.15$ at $t = 64$ days, while in the initially crystalline configuration $0.00 \leq f_{cl} \leq 0.02$. At $t = 81$ days, when the initially glassy configuration had crystallised, f_{cl} had dropped to 0.01. During the first 64 days the crystalline fraction in the initially glassy configuration increased very slowly from $f_X = 0.00$ to $f_X = 0.02$ (as shown in the inset of Fig. 3b), before making a large jump to $f_X = 0.98$ at $t = 81$ days. Clearly, the crystalline configurations contain significantly fewer clusters (~a few percent) than the glassy configurations (~tens of percents), regardless of the initial structure of the crystalline configuration.

From these observations we conclude that a clustered fraction f_{cl} above a certain threshold value prevented crystallisation. When the particles were pressed together by the centrifugal field, clusters were formed in the dense part of the sediment. After centrifugation, when the sample was kept in gravity, the dense part of the sediment expanded and subsequently, during a long time, the number of clusters decreased. Finally, after 64–81 days, the clusters almost completely disappeared by spontaneous dissociation. In order to elucidate the mechanism of clustering and the subsequent declustering we investigated this phenomenon separately, as described in Section 3.5. Up to $t = 64$ days the f_{cl} was sufficiently high to allow only a very small fraction of the particles to become crystalline. At some point during the time period $t = 64$–81 days, when f_{cl} dropped below a threshold value (which must be somewhere between 0.15 and 0.01), crystallisation was no longer frustrated, and almost the entire system was able to crystallise. The lowest f_{cl} observed for a glass (structure with $f_X < 0.05$) was 0.12; so, apparently, $f_{cl} = 0.12$ was sufficient to frustrate crystallisation.

At this point it is interesting to compare with the glassy states found in ref. 27, in a system which bears resemblance to our system, having long-range electrostatic repulsions, but in addition short-range depletion interactions. For the system in ref. 27, when the polymer concentration was zero, and the interactions purely repulsive, a glassy state existed across the entire volume fraction range ($\eta = 0$–0.55). For $\eta > 0.2$ sometimes a crystal was found. Attractions were introduced in the system by increasing the polymer concentration, resulting in the formation of a cluster glassy state at low volume fractions (roughly for $0.02 < \eta < 0.12$) and a gel state at high volume fractions. For our system the situation is different: in the absence of any clusters, we always found a crystalline phase for $\eta > 0.02$. To form the glassy state, the presence of clusters was essential. This difference in behaviour might be due to differences in the range or strength of (the repulsive part of) the interaction potential.

We looked in more detail at the size of the clusters present in the sample. We calculated the cluster size distributions, and found that most of the clusters were dumbbells, the fraction in the glassy parts of the sample increasing from ~75% at $t = 7$ days to ~86% at $t = 64$ days. Only a small number of clusters consisted of more than four particles, their fraction decreasing from ~3% to ~1% during the same period.

Fig. 4 shows a glassy part of the sample at $t = 21$ days, for which we indicated the clusters found by our distance criterion. We recorded a sequence of 25 images with time step $\Delta t = 120$ s. In Fig. 4 (left) the average intensity of the 25 images is shown. It is clear from the average intensity that the system was dynamically arrested, as the particle positions hardly changed over the course of 48 minutes. We obtained the locations of the clusters from a three-dimensional dataset taken at the same *xy* position; the clustered particles that are part of clusters for which more than one member is visible in the image are indicated by blue circles (Fig. 4, right). The clustered particles can also be recognised in the corresponding movie† from the correlated motion of the particles. From the motion of the particles one identifies the same clusters as found by the distance criterion we used. The movie shows that the particles were able to move over small distances (cage-rattling motion), but almost all remained confined to the cage formed by their neighbours on the timescale of the movie (48 minutes).

In the ESI† we included another movie, which was recorded for an even longer time frame of 12 hours in a typical sample that had been centrifuged for 10 minutes at 42*g* five hours prior to the start of the movie. Apart from a few isolated particle

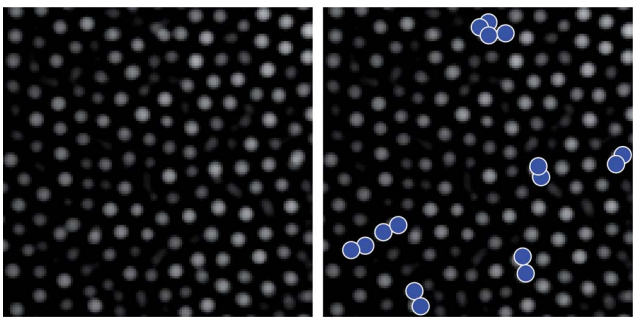

Fig. 4 Long-term structural arrest in a glassy part of the sample at $t = 21$ days with $\eta = 0.17$, $f_X = 0.01$ and $f_{cl} = 0.15$. Images show the average intensity of a series of 25 confocal images (42.5 μm × 42.5 μm) taken at the same position in the sample, but at different points in time. Images were taken with a time step $\Delta t = 120$ s. On the right we indicate the clustered particles (blue circles) found by distance analysis of a three-dimensional dataset, taken at the same *xy* position in the sample. The corresponding movie is available in the ESI.†

rearrangements and a 'plug flow' that caused the structure to move with respect to the field of view, there was clearly hardly any particle mobility. From this we conclude that the samples were glassy on the timescale of our observation (12 hours).

When an image stack is recorded at a certain position in the sample, the particles in that location are bleached. This provided us with a method to establish dynamic arrest in the system over a longer period of time. At a given measurement day we could still identify the areas containing particles that were bleached due to imaging on the previous measurement day, next to areas that contained brighter particles. For example, in a confocal image recorded at $t = 14$ days, we were able to identify a bleached area that resulted from imaging that had taken place at least a week before (at $t = 7$ days), as no imaging of the sample was done between $t = 7$ days and $t = 14$ days, indicating clearly that the system was dynamically arrested on this timescale (7 days).

3.3. Structural analysis of the glasses

Fig. 5 shows the radial distribution function $g(r)$ for three long-range repulsive glasses (corresponding to the data points in Fig. 3b at $t = 7$, 21 and 64 days). For comparison, we also show the $g(r)$ determined experimentally in a glassy system of silica spheres which interact as effective hard spheres (see Section 2.1). The radial distribution functions for the long-range repulsive glasses have been rescaled such that their maxima and minima coincide with those of the hard-sphere glass. For the hard-sphere glass we found a split second peak, similar to that found before for hard-sphere glasses.[10,58–60] The left and right subpeaks correspond to different local particle arrangements; both correspond to a pair of particles that are in each other's second-neighbour shell, but have either three first neighbours (left subpeak) or one first neighbour (right subpeak) in common.[61] Their relative heights vary according to the local structure, which depends on the system's characteristics, *e.g.* its polydispersity and the type of particles.[61,62] For the long-range repulsive glasses, we found a second peak with a shoulder to its right. The small peak to the left of the main peak, present for the long-range repulsive glasses, is due to the clustered particles.

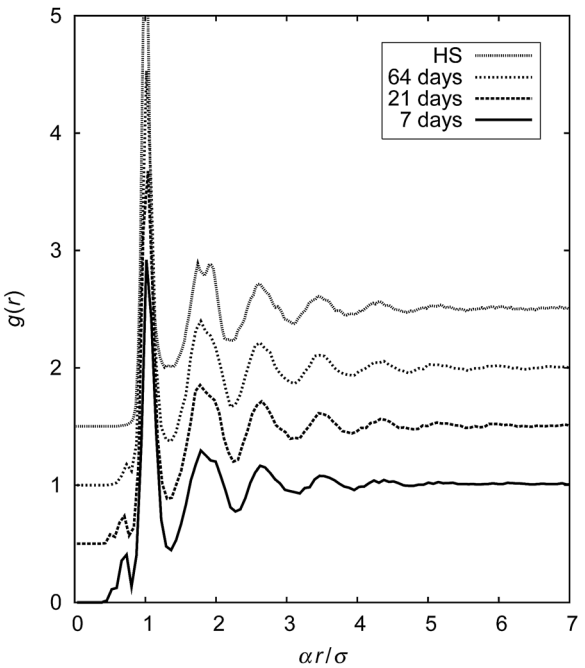

Fig. 5 Radial distribution function $g(r)$ for three long-range repulsive glasses (corresponding to the data points in Fig. 3b; $t = 7$ days, $\eta = 0.22$, $f_X = 0.00$, $f_{cl} = 0.37$; $t = 21$ days, $\eta = 0.20$, $f_X = 0.01$, $f_{cl} = 0.21$; $t = 64$ days, $\eta = 0.23$, $f_X = 0.02$, $f_{cl} = 0.15$). The $g(r)$ for a hard-sphere glass is also shown for comparison ($\eta = 0.64$, $f_X = 0.01$). The radial distribution functions for the long-range repulsive glasses have been rescaled, with $\alpha = 0.70$, 0.67 and 0.70, respectively, for $t = 7$, 21 and 64 days; for the hard-sphere glass $\alpha = 1$. For clarity, the three upper curves have been shifted vertically.

Fig. 6a shows the $\hat{w}_6$ probability distribution for the three long-range repulsive glasses and the hard-sphere glass. The distributions were calculated using the Voronoi construction to define the neighbours (see Section 2.3) in order to make a comparison with the structure of hard-sphere glasses as published in ref. 10. The same distributions calculated using a cut-off of $1.5\rho^{-1/3}$ to define the neighbours were very similar to the distributions shown in Fig. 6a; using those instead would not change the conclusions.

Despite the large difference in volume fraction and particle interactions between the long-range repulsive and hard-sphere glasses, the local bond-orientational order is remarkably similar. The distributions fall on top of each other within error. The differences in the local bond order between the long-range repulsive glasses at different waiting times were similar to the differences between two glasses from the same sample, imaged at the same day. Also, the difference between the long-range repulsive glasses and the hard-sphere glass is in the same range. We find good correspondence with the $\hat{w}_6$ distribution for the hard-sphere glass from the literature.[10] In ref. 13 it was found in a colloidal system with short-range attractions that the $\hat{w}_6$ distributions for the liquid and gel phases were very similar. Nevertheless, a cluster-based structural analysis revealed significant differences in the local structure. It would therefore be interesting to explore in future work whether it is possible to find structural differences between our glasses by using this cluster-based method.

In Fig. 6b we plotted the probability distribution $P(n_n)$ for the number of neighbours surrounding a particle. Since we used here the Voronoi construction to define the neighbours, this is the same as the number of faces of the Voronoi cell in which the particle is contained. Fig. 6c depicts the probability distribution $P(n_e)$ for the number of particles surrounding a bond, which is the same as the number of edges of the Voronoi face corresponding to this bond. These distributions are again very similar for the long-range repulsive glasses and the hard-sphere glass, and also very similar to the same distributions in ref. 10.

Fig. 7 illustrates crystallisation in a long-range repulsive glass at one particular spot in the sediment, indicated in Fig. 2 by black squares. The configurations at $t = 21$ and 64 days were glassy; they correspond to the glasses in Fig. 5 and 6 at the same waiting times. At $t = 81$ days the system had crystallised. For comparison the hard-sphere glass is shown as well. On the left

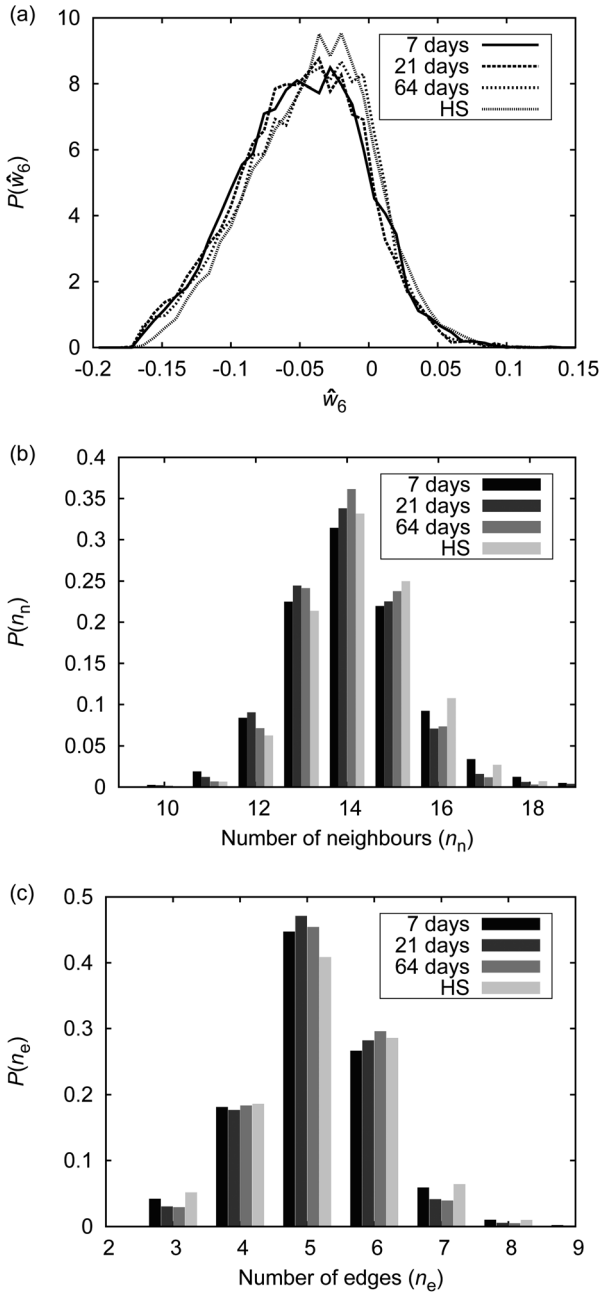

Fig. 6 (a) Probability distribution of the bond-orientational order parameter $\hat{w}_6$, (b) probability distribution of the number of Voronoi neighbours per particle n_n and (c) probability distribution of the number of edges surrounding a Voronoi face n_e, for three long-range repulsive glasses and a hard-sphere glass (corresponding to the data points in Fig. 3b; for details see Fig. 5).

the colour of the particles is related to the bond-orientational order parameter $\bar{q}_6$: particles with low $\bar{q}_6$ are purple, particles with high $\bar{q}_6$ are red. On the right the particles were given a colour according to their crystallinity: crystalline particles are red and drawn at full size, fluid particles are cyan and (for clarity) drawn with a size equal to half their actual diameter. The $\bar{q}_6$ order parameter is a good measure for the local bond order, it tends to higher values when the local order resembles bcc or fcc crystalline order and to lower values when the local order is glass- or fluid-like.[57] $\bar{q}_6$ includes the averaged bond order of the central particle and the particles in its first-neighbour shell (Section 2.3, eqn (11)), thereby directly depending on the positions of the particles in the second-neighbour shell. To average out the effect of thermal fluctuations,[55] it was necessary to use the $\bar{q}_6$ instead of the more local q_6 order parameter, which depends only on the position of the particles in the first-neighbour shell. The reconstructions show that each glass (long-range repulsive and hard-sphere) had regions of high and low local bond order, and that, as expected, the regions containing crystalline particles had the highest local bond order. The reconstructions illustrate that the number of crystalline particles in the long-range repulsive glass very slowly increased in time until $t = 64$ days, and that the system at $t = 81$ days was almost fully crystalline. The local bond order in the long-range repulsive glasses closely resembled the local bond order in the hard-sphere glass, despite the significant difference in the volume fractions of these systems.

3.4. Structural analysis of the crystals

The equilibrium phase diagram for colloidal systems interacting through a hard-core repulsive Yukawa pair potential contains two crystal phases; these are the body-centred-cubic (bcc) and the face-centred-cubic (fcc) crystal phase.[63–65] On going from low to high volume fraction, it is possible to find (i) a fluid phase followed by an fcc crystal phase (for small screening lengths) or (ii) a fluid phase, followed by a bcc crystal phase and then an fcc crystal phase (for larger screening lengths). The phases are separated by relatively narrow coexistence regions. In more recent work Yukawa phase diagrams were calculated under the constant-potential assumption and charge-regulation conditions,[38] instead of for a fixed contact value of the interaction potential as before.[63–65] Again, the phase diagram contained fluid, bcc and fcc regions, but the crystals were stable in a much smaller part of the phase diagram. Discharging of the colloids with increasing volume fraction and decreasing salt concentration gave rise to a re-entrant fluid phase at high volume fraction and a stable fluid phase across the entire volume fraction range at low salt concentration.

For some combinations of Yukawa parameters the difference in free energy between an fcc crystal and a hexagonal-close-packed (hcp) crystal is very small,[66] and it is not uncommon to find a random stacking of close-packed layers under conditions where the equilibrium crystal phase is fcc.[33,67–69] This structure is referred to as the random-hexagonal-close-packed (rhcp) crystal.

The phase behaviour is determined by system parameters Z and $(\kappa\sigma)^{-1}$, and we can extract rough estimates for the system parameters from the observed phase behaviour.

We used the bond order parameter $\bar{w}_6$ to distinguish between particles that are in an fcc or hcp environment and particles that are in a bcc environment (similar to ref. 55). In an ideal crystal with only one type of lattice site, $\bar{w}_6$ will have the same value as $\hat{w}_6$, which is negative for fcc and hcp crystals (-0.0131 and -0.0124, respectively), and positive for bcc crystals (0.0131).[54] On this basis we assumed that crystalline particles which had $\bar{w}_6 < 0$ were in an fcc, hcp or intermediate

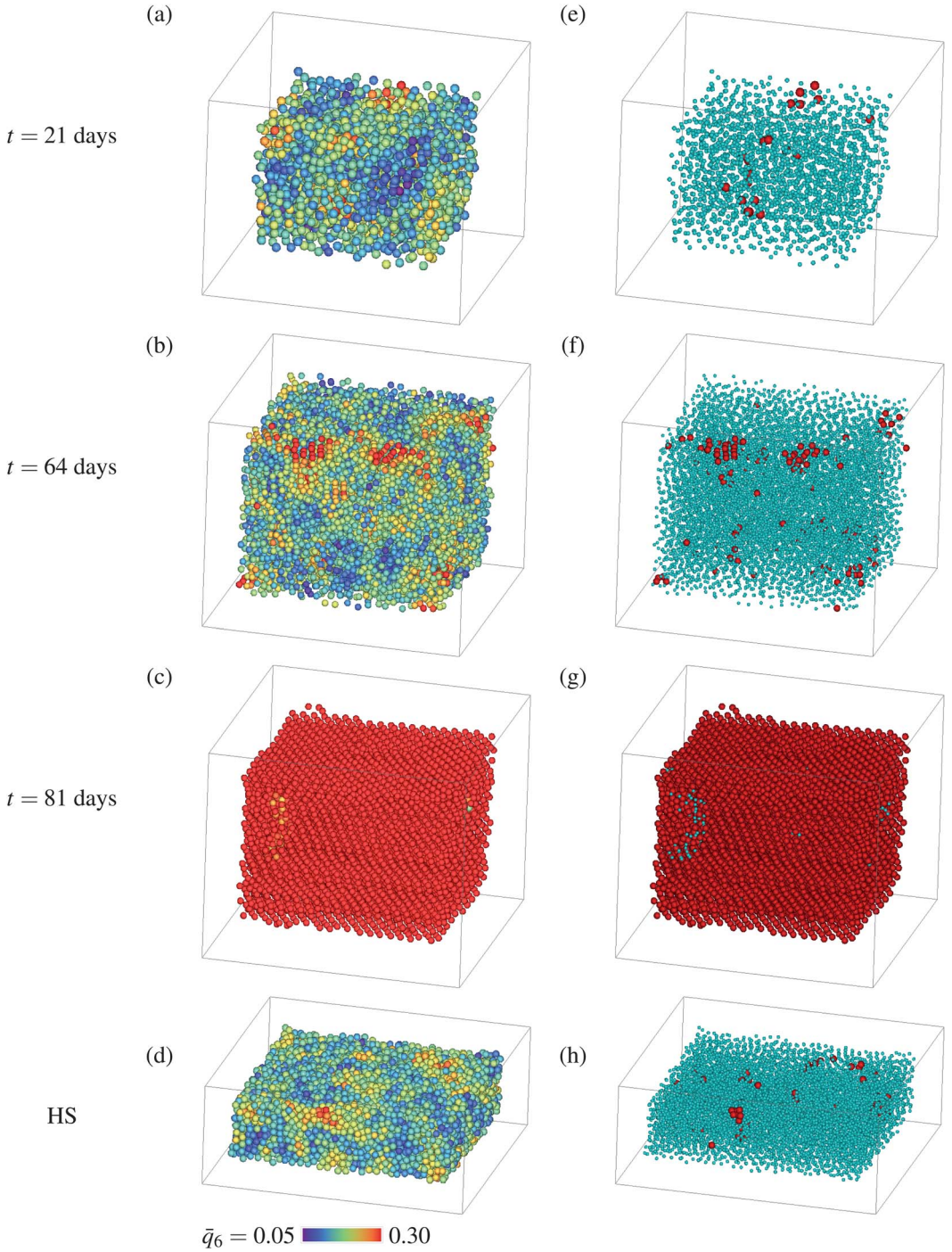

Fig. 7 3D reconstructions showing crystallisation in an initially glassy part of the sample at $t = 21$, 64 and 81 days and a hard-sphere glass (long-range repulsive configurations corresponding to the data points in Fig. 3b; $t = 81$ days, $\eta = 0.22$, $f_X = 0.98$, $f_{cl} = 0.01$; for details of the glassy configurations see Fig. 5). (a)–(d) Colour according to local bond order parameter $\bar{q}_6$; purple = low $\bar{q}_6$, red = high $\bar{q}_6$. (e)–(h) Same configurations as (a)–(d) but now red particles are crystalline, cyan particles are non-crystalline. For clarity, the diameter of the non-crystalline particles is equal to half the actual diameter.

environment and crystalline particles which had $\bar{w}_6 > 0$ were in a bcc environment. In the following we will refer to fcc, hcp and in-between particles simply as fcc. The $\bar{w}_6$ distributions that we calculated for our crystalline systems indeed showed peaks close to one or both of these values, representing the most crystalline particles in the system. As mentioned above, we used $\bar{w}_6$ instead of $\hat{w}_6$ to reduce the effect of thermal fluctuations.

Up to $t = 7$ days the crystalline particles were predominantly bcc (Fig. 8a). At $t = 14$ and 21 days we found a mixture of bcc and fcc regions (Fig. 8b). The crystalline regions adjacent to the bulk glass phase (on the left side of the profiles in Fig. 2) or surrounding crystal defects, tended to contain more bcc particles. From $t = 35$ to 81 days the crystalline particles were predominantly fcc (Fig. 8c), except in a small region close to the

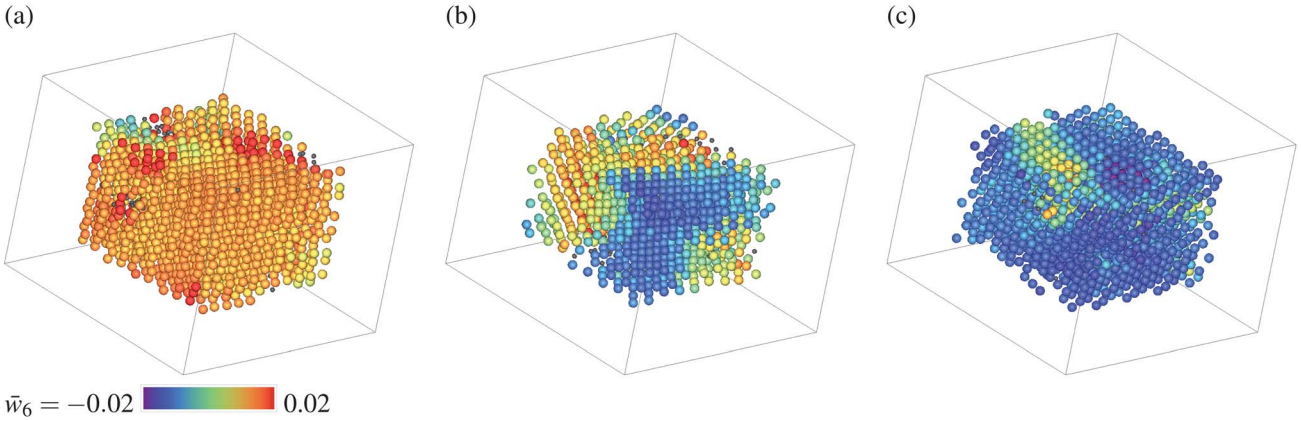

Fig. 8 Crystalline configurations from Fig. 3c at (a) $t = 2$ days ($\eta = 0.18$, $f_X = 0.91$, $f_{cl} = 0.04$), (b) $t = 14$ days ($\eta = 0.13$, $f_X = 0.97$, $f_{cl} = 0.004$) and (c) $t = 35$ days ($\eta = 0.17$, $f_X = 0.97$, $f_{cl} = 0.02$). For the crystalline particles, the colour indicates the value of bond order parameter $\bar{w}_6$; bcc-like particles are orange and fcc-like particles are blue; non-crystalline particles are grey and reduced in size (to half the actual diameter).

bulk glass phase, where the majority of crystalline particles was bcc-like.

At each point in time after centrifugation the sample displayed fluid–crystal coexistence close to one end of the sediment (furthest from the water–CHB interface). In Fig. 9 we plotted the volume fraction at the fluid–crystal boundary (the freezing volume fraction η_f). We left out the data points for $t < 2$ days, because the particles were then still migrating towards the interface. We also indicated the crystalline environment of the majority of particles found close to the fluid interface. We found a fluid–bcc transition for $t \leq 14$ days and a fluid–fcc transition for $t \geq 35$ days.

The sample was crystalline across a broad volume fraction range (from η_f up to $\eta = 0.16$–0.21, where the system was glassy). For all waiting times the structure of the crystalline regions (bcc, mixed or fcc) was quite homogeneous across almost the entire crystalline part of the sediment. A systematic dependence of the crystal symmetry on the local volume fraction was not found. Most inhomogeneous with regard to crystal symmetry was the sample at $t = 14$ days, for which we found a fluid–bcc coexistence, but at higher volume fraction a mixture of bcc and fcc regions (Fig. 8).

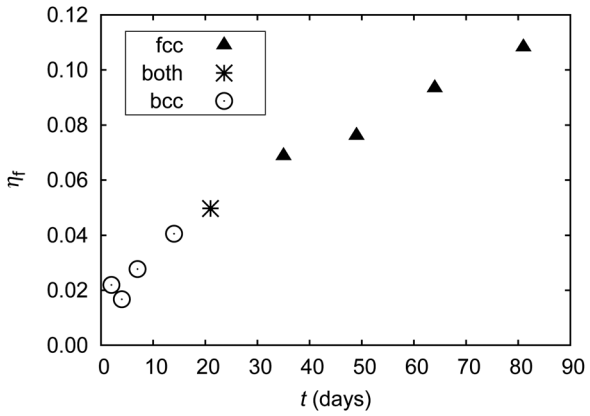

Fig. 9 Freezing volume fraction η_f as a function of time t.

Somewhere between $t = 14$ and 35 days the system changed from having a fluid–bcc to having a fluid–fcc transition, and therefore must have passed a triple point where the three phases (fluid, bcc and fcc) coexisted. We estimated the volume fraction of this triple point to be $\eta_t \approx 0.05$ and to occur around $t = 21$ days. The triple point of hard-core repulsive Yukawa systems can be well mapped onto the triple point of Yukawa systems.[65,70] The value η_t is determined by a unique combination of particle surface potential ψ_0 (or charge number Z) and Debye screening length $(\kappa\sigma)^{-1}$. We calculate at the triple point: $(\kappa\sigma)^{-1} \approx 0.3$ and $\beta e\psi_0 \approx 2$, corresponding to a charge number of $Z \approx 8 \times 10^2$.[65,70] The increase of η_f in time and the change from fluid–bcc to fluid–fcc coexistence indicate a change of the particle interactions. When we assume a constant $(\kappa\sigma)^{-1} \approx 0.3$, the surface potential $\beta e\psi_0$ has to change from ~7 to ~1 in order to access the range of freezing volume fractions $\eta_f = 0.02$–0.11; the corresponding charge numbers would be $Z \approx 3 \times 10^3$ to 4×10^2. When we assume the surface potential $\beta e\psi_0 \approx 2$ to be constant, the screening length $(\kappa\sigma)^{-1}$ has to vary between ~0.8 and ~0.1. These limiting values for $\beta e\psi_0$ and $(\kappa\sigma)^{-1}$ were calculated from the fit to the fluid–bcc phase boundary, given in ref. 65 (see also ref. 70). In reality, presumably a combination of these two effects occurred.

We can use the results from ref. 38 to narrow down the estimate for $(\kappa\sigma)^{-1}$ in our system. Interactions are determined by $\beta\varepsilon$ and $(\kappa\sigma)^{-1}$ (eqn (1)). For our system, $\beta e\psi_0 = 2$ and $\lambda_B/\sigma = 0.0032$, so, from eqn (7), $\beta\varepsilon = 3.1 \times 10^2$. In ref. 38, with $\lambda_B/\sigma = 0.005$, $\beta\varepsilon = 3.1 \times 10^2$ corresponds to $\beta e\psi_0 = 2.5$. In Fig. 3b and c of ref. 38 the constant-potential and charge-regulated phase diagrams are plotted for $\beta e\psi_0 = 2$ and $\beta e\psi_0 = 3$; the phase diagram for $\beta e\psi_0 = 2.5$, which would correspond to our system, is the intermediate between these two. The constant-potential phase diagram shows that for $\eta = 0.3$ the maximum $(\kappa\sigma)^{-1}$ at which the crystal still exists is ~0.6 and ~1.0, for $\beta e\psi_0 = 2$ and 3, respectively. For the charge-regulated phase diagram these values for the maximum $(\kappa\sigma)^{-1}$ at which the crystal still exists are higher. This means that even for the highest $(\kappa\sigma)^{-1}$ we estimated for our system ($(\kappa\sigma)^{-1} = 0.8$) no re-entrant melting is

yet expected. However, for high $\beta e\psi_0$ and/or high η the interactions are better described by an effective screening length. When we consider the phase diagram for $\beta e\psi_0 = 2$ plotted in terms of the effective screening length, as depicted in Fig. 5 of ref. 38, we see that for $\eta = 0.3$ the maximum *effective* screening length at which the crystal still exists is ~0.4 for $\beta e\psi_0 = 2$ (the plot for $\beta e\psi_0 = 3$ is not shown, but the value for the effective screening length is presumably slightly larger than for $\beta e\psi_0 = 2$). As we did not observe re-entrant melting in our system, this finding indicates an upper limit for $(\kappa\sigma)^{-1}$. We conclude that the lowest $\eta_f = 0.02$ was at least partly due to a higher $\beta e\psi_0$ on the colloids. Below (Section 3.5) we argue that the assumption of a decreasing $(\kappa\sigma)^{-1}$ is necessary in order to account for the spontaneous cluster dissociation that was observed.

We note that close to the bulk glass phase we observed bcc crystals for samples with a fluid–fcc coexistence (for $t = 35$–81 days, as mentioned above). However, for $(\kappa\sigma)^{-1}$ below that of the triple point, bcc crystals do not exist across the entire volume fraction range.[38,65] The observation of bcc crystals (close to the bulk glass phase) and a fluid–fcc transition in the same sample could be explained by slightly changing the particle interactions as a function of distance from the water–CHB interface and/or a stabilisation of the bcc crystals with respect to fcc crystals by the adjacent amorphous bulk glass phase.

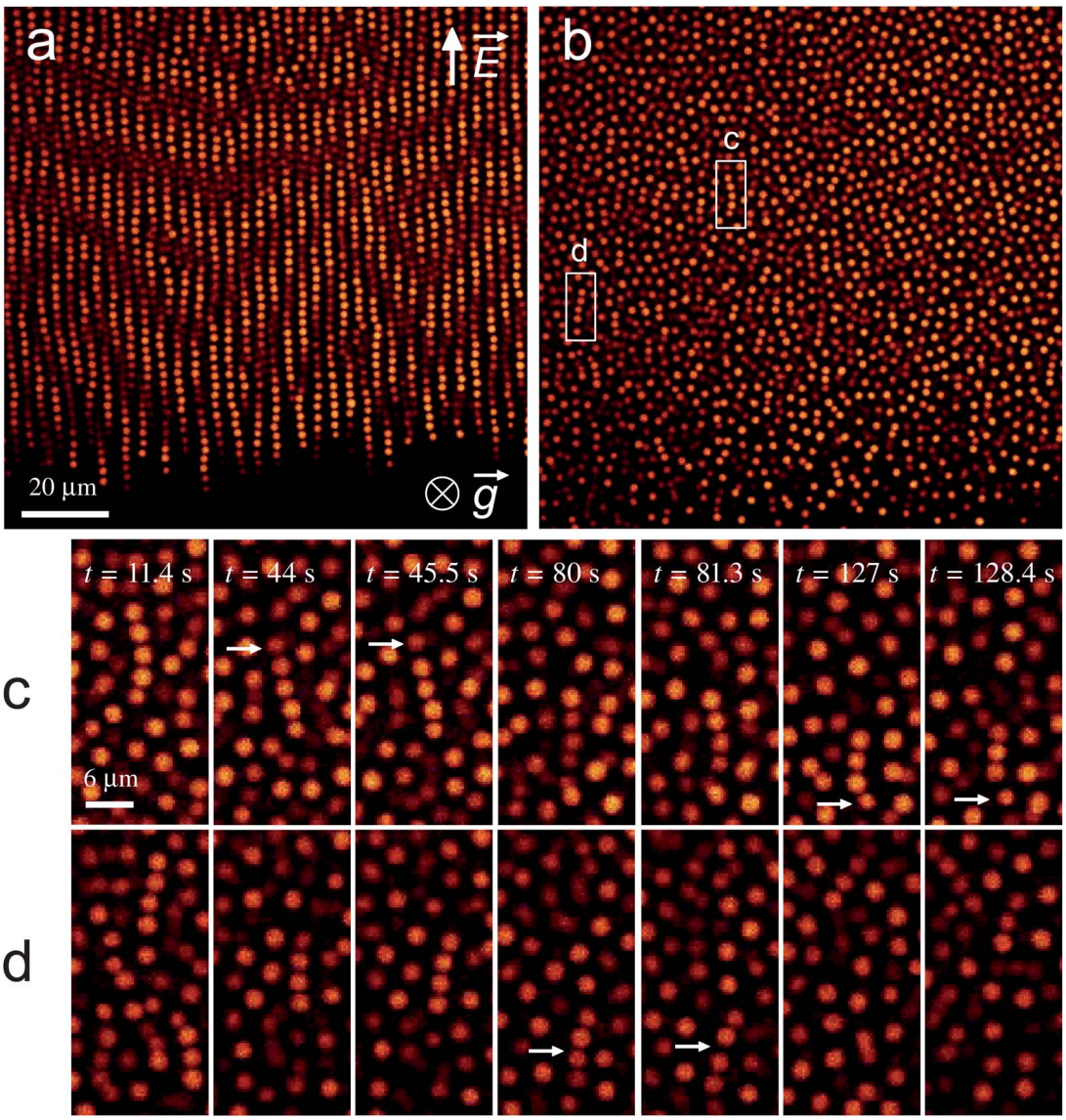

Fig. 10 Confocal images of PMMA particles ($\sigma = 2.23$ μm) in CHB forming strings under an AC electric field. (a) PMMA strings after 10 minutes of waiting time. (b) The sample after switching off the *E*-field: small strings persisted for a certain time before breaking. Series (c) and (d) show the breaking process for two different strings of lengths five and four particles, respectively (indicated by the white rectangles in image (b)). In series (c) the top particle of the string separated from the rest 45 seconds after switching off the *E*-field, as indicated by the white arrows. A second particle (the bottom one) in the string separated after more than 2 minutes of observation. In series (d) the string divided into two dumbbells 81 seconds after the field was turned off. The corresponding movies are available in the ESI.†

3.5. Origin of the attractions

To understand the origin of the cluster formation and the subsequent disappearance of the clusters better, we performed additional experiments. Instead of concentrating the system by centrifugation, we used an external electric field to bring particles into contact and observed the system after switching off the field.

When an electric field is applied to a colloidal suspension in which the dielectric constant of the particles is different from that of the suspending medium (here: at 1 MHz, $\varepsilon_r = 2.6$ for PMMA, $\varepsilon_r = 7.92$ for CHB), the particles acquire a dipole moment, causing them to align in strings parallel to the *E*-field. The total interaction between particles is a sum of the hard-core repulsive Yukawa interaction and an induced long-range dipolar interaction.[28,30,52,71–73]

Upon application of an AC external electric field (root-mean-square amplitude $E_{rms} = 0.4$ V μm^{-1}, frequency $f = 1$ MHz) to a suspension of our PMMA particles in CHB ($\eta \approx 0.02$), the particles assembled into strings parallel to the *E*-field direction (see Fig. 10a). We note that at some places inside the strings a small separation can be seen between two particles within the same string (Fig. 10a), due to the strong repulsive electrostatic force between particles. After a waiting time of 10 minutes, during which the *E*-field was on, we switched off the field and followed the breaking up of strings using confocal microscopy. Fig. 10c and d show this process for two different strings (lengths of five and four particles, respectively), located at different places in the sample, as indicated by the white rectangles in Fig. 10b. In the first series (Fig. 10c) the top particle of a string of five particles separated from the remaining four particles 45 seconds after switching off the *E*-field. A second particle (the bottom one) in the string separated after more than 2 minutes of observation. In the second series (Fig. 10d) a string of four particles divided into two dumbbells 81 seconds after the field was turned off. We could not follow the separation of the particles in the remaining dumbbells because the particles moved out of the plane of observation. After a long waiting time (one day in this case), all clusters had disappeared and only single particles were observed in the sample.

We seek the origin of the attractive interactions between the particles in the attractions between PMMA chains that also keep an uncross-linked particle together (mostly Van der Waals attractions). We think these attractions come into play when PMMA chains are brought into direct contact as the particles are pressed together by the centrifugal or electric field and are thus responsible for cluster formation in our systems.

The *E*-field experiments described in this section demonstrate that pressing particles together results in the formation of clusters and that, with time, the clusters spontaneously dissociate. The difference in timescale on which the clusters disappear (minutes to hours for the *E*-field *versus* several months for the centrifugation experiments) could be due to many different parameters, such as the force with which the particles were pressed together, the duration of the compression, the details of the particle interactions at close contact and further away, and the volume fraction ($\eta = 0.02$ *versus* up to $\eta = 0.64$).

The centrifugal field exerts a force of approximately 1×10^{-13} N on each particle (calculated from: particle volume × effective density × acceleration $= \pi\sigma^3/6 \times (d_{CHB} - d_{PMMA}) \times 15g$, with $\sigma = 2.23$ μm, $d_{CHB} = 1.336$ g cm^{-3}, $d_{PMMA} = 1.19$ g cm^{-3} and $g = 9.8$ m s^{-2}). Apparently, this field is sufficiently strong to push the particles not only through the double layer but also through the steric stabilising layer. The former is understandable as the force from the long-range repulsive potential at a distance of 10 nm between the surfaces of the two spheres is 1×10^{-12} N for interaction parameters of $(\kappa\sigma)^{-1} = 1.0$ and $\beta e\psi_0 = 2.0$, and several layers of particles are pressing down on the densest part of the sediment where the clusters are formed. With time, as the ionic strength increases and the double layer becomes more compressed, the repulsive potential becomes steeper and the resulting forces become strong enough to break up the clusters. For a double-layer thickness of $(\kappa\sigma)^{-1} = 0.1$ the repulsive forces at the same surface-to-surface interparticle distance of 10 nm, which is approximately twice the thickness of the steric stabilising layer, have increased to 6×10^{-12} N. We note that assuming a constant $(\kappa\sigma)^{-1}$ and decreasing ψ_0 to account for the observed range of freezing volume fractions would result in a decreasing force with time and would not explain the cluster dissociation.

4. Conclusions

Compression by centrifugation of a dilute suspension ($\eta \approx 0.02$) of charged PMMA colloids in CHB resulted in the formation of long-range repulsive glasses at volume fractions $\eta \geq 0.16$. Crystallisation of the long-range repulsive glasses was prevented by the presence of small clusters (mostly dumbbells), which were formed during the centrifugation step. Spontaneous dissociation of the clusters brought the number of clustered particles down. For more than two months, the number of crystalline particles in the system (~25% of the total number of particles) did not change, while the number of clustered particles decreased but settled at ~13%. Only after $t = 81$ days we found extensive crystallisation in the formerly glassy parts of the system, with ~88% of the total number of particles crystalline and ~3% clustered.

A clustered fraction f_{cl} of 0.12 was sufficiently high to completely frustrate crystallisation in our system. In previous work[74] we used computer simulations to investigate the effect of size polydispersity in systems with $\beta e\psi_0 \approx 2$ and $(\kappa\sigma)^{-1} = 0.1$–0.4, comparable to the system used in the present work. We found that a polydispersity s of 0.13 frustrated crystallisation in parts of the system; for $s = 0.15$ this effect was stronger, resulting in a lower overall crystalline fraction. The non-crystalline parts were found to be glassy, judged from the very slow dynamics that they exhibited. We calculated the polydispersity separately for the crystalline and glassy parts; interestingly, the glassy parts had a higher polydispersity than the crystalline parts. This is similar to the results in the current work: the glassy parts have a higher f_{cl} than the crystalline parts. The difference is that in ref. 74 crystallisation was frustrated by size polydispersity, while in the current work it is due to the presence of small clusters.

The system parameters changed in time causing the system to pass the fluid-bcc-fcc triple point around $t = 21$ days with $\eta_t \approx 0.05$. From this we obtained rough estimates for the Debye screening length $(\kappa\sigma)^{-1} \approx 0.3$ and surface potential $\beta e\psi_0 \approx 2$ (charge number $Z \approx 8 \times 10^2$). To account for the observed range of freezing volume fractions $\eta_f = 0.02$–0.11, we must assume that either the screening length or the surface potential (or both) have changed for the waiting period of 81 days.

Finally, it is truly surprising that we did not find any significant changes in the structure of the glass, despite the large range of volume fractions and changing system parameters. We compared to hard-sphere data, and found good agreement between the local bond-orientational orders in the long-range repulsive glasses and the hard-sphere glass.

Acknowledgements

We would like to thank Gulşen Heessels-Gürboğa for synthesis of the PMMA particles, Anke Kuijk for synthesis of the silica particles, Johan Stiefelhagen for help with the locking procedure and Michiel Hermes for sharing his code for obtaining particle coordinates. Part of this work was supported by NWO-SRON. MNvdL acknowledges the support of an NWO-Toptalent grant from the Netherlands Organisation for Scientific Research (NWO).

References

1 W. B. Russel, D. A. Saville and W. R. Schowalter, *Colloidal dispersions*, Cambridge University Press, Cambridge, 1992.
2 P. N. Pusey and W. van Megen, *Phys. Rev. Lett.*, 1987, **59**, 2083–2086.
3 W. van Megen and S. M. Underwood, *Phys. Rev. E: Stat. Phys., Plasmas, Fluids, Relat. Interdiscip. Top.*, 1994, **49**, 4206–4220.
4 A. H. Marcus, J. Schofield and S. A. Rice, *Phys. Rev. E: Stat. Phys., Plasmas, Fluids, Relat. Interdiscip. Top.*, 1999, **60**, 5725–5736.
5 W. K. Kegel and A. van Blaaderen, *Science*, 2000, **287**, 290–293.
6 E. R. Weeks, J. C. Crocker, A. C. Levitt, A. Schofield and D. A. Weitz, *Science*, 2000, **287**, 627–631.
7 F. Sciortino and P. Tartaglia, *Adv. Phys.*, 2005, **54**, 471–524.
8 P. N. Pusey and W. van Megen, *Nature*, 1986, **320**, 340–342.
9 G. Brambilla, D. El Masri, M. Pierno, L. Berthier, L. Cipelletti, G. Petekidis and A. B. Schofield, *Phys. Rev. Lett.*, 2009, **102**, 085703.
10 A. van Blaaderen and P. Wiltzius, *Science*, 1995, **270**, 1177–1179.
11 L. Berthier and G. Biroli, *Rev. Mod. Phys.*, 2011, **83**, 587–645.
12 A. Cavagna, *Phys. Rep.*, 2009, **476**, 51–124.
13 C. P. Royall, S. R. Williams, T. Ohtsuka and H. Tanaka, *Nat. Mater.*, 2008, **7**, 556–561.
14 M. Leocmach and H. Tanaka, *Nat. Commun.*, 2012, **3**, 974.
15 H. Tanaka, T. Kawasaki, H. Shintani and K. Watanabe, *Nat. Mater.*, 2010, **9**, 324–331.
16 T. Kawasaki and H. Tanaka, *J. Phys.: Condens. Matter*, 2010, **22**, 232102.
17 J. Taffs, S. R. Williams, H. Tanaka and C. P. Royall, *Soft Matter*, 2013, **9**, 297–305.
18 D. Coslovich and G. Pastore, *J. Chem. Phys.*, 2007, **127**, 124504.
19 A. Di Cicco, A. Trapananti, S. Faggioni and A. Filipponi, *Phys. Rev. Lett.*, 2003, **91**, 135505.
20 P. Wochner, C. Gutt, T. Autenrieth, T. Demmer, V. Bugaev, A. Diaz Ortiz, A. Duri, F. Zontone, G. Grübel and H. Dosch, *Proc. Natl. Acad. Sci. U. S. A.*, 2009, **106**, 11511–11514.
21 E. B. Sirota, H. D. Ou-Yang, S. K. Sinha, P. M. Chaikin, J. D. Axe and Y. Fujii, *Phys. Rev. Lett.*, 1989, **62**, 1524–1527.
22 W. Härtl, H. Versmold and X. Zhang-Heider, *J. Chem. Phys.*, 1995, **102**, 6613–6618.
23 Ch. Beck, W. Härtl and R. Hempelmann, *J. Chem. Phys.*, 1999, **111**, 8209–8213.
24 F. Ebert, P. Keim and G. Maret, *Eur. Phys. J. E: Soft Matter Biol. Phys.*, 2008, **26**, 161–168.
25 S. Mazoyer, F. Ebert, G. Maret and P. Keim, *Eur. Phys. J. E: Soft Matter Biol. Phys.*, 2011, **34**, 101.
26 J. Mattsson, H. M. Wyss, A. Fernandez-Nieves, K. Miyazaki, Z. Hu, D. R. Reichman and D. A. Weitz, *Nature*, 2009, **462**, 83–86.
27 C. L. Klix, C. P. Royall and H. Tanaka, *Phys. Rev. Lett.*, 2010, **104**, 165702.
28 A. Yethiraj and A. van Blaaderen, *Nature*, 2003, **421**, 513–517.
29 C. P. Royall, M. E. Leunissen and A. van Blaaderen, *J. Phys.: Condens. Matter*, 2003, **15**, S3581–S3596.
30 D. El Masri, T. Vissers, S. Badaire, J. C. P. Stiefelhagen, H. R. Vutukuri, P. Helfferich, T. H. Zhang, W. K. Kegel, A. Imhof and A. van Blaaderen, *Soft Matter*, 2012, **8**, 6979–6990.
31 C. P. Royall, M. E. Leunissen, A.-P. Hynninen, M. Dijkstra and A. van Blaaderen, *J. Chem. Phys.*, 2006, **124**, 244706.
32 S. Hachisu and K. Takano, *Adv. Colloid Interface Sci.*, 1982, **16**, 233–252.
33 J. S. van Duijneveldt, J. K. G. Dhont and H. N. W. Lekkerkerker, *J. Chem. Phys.*, 1993, **99**, 6941–6949.
34 D. El Masri, P. van Oostrum, F. Smallenburg, T. Vissers, A. Imhof, M. Dijkstra and A. van Blaaderen, *Soft Matter*, 2011, **7**, 3462–3466.
35 S. K. Sainis, V. Germain, C. O. Mejean and E. R. Dufresne, *Langmuir*, 2007, **24**, 1160–1164.
36 T. Vissers, A. Imhof, F. Carrique, A. V. Delgado and A. van Blaaderen, *J. Colloid Interface Sci.*, 2011, **361**, 443–455.
37 D. Reinke, H. Stark, H.-H. von Grünberg, A. B. Schofield, G. Maret and U. Gasser, *Phys. Rev. Lett.*, 2007, **98**, 038301.
38 F. Smallenburg, N. Boon, M. Kater, M. Dijkstra and R. van Roij, *J. Chem. Phys.*, 2011, **134**, 074505.
39 R. van Roij and J.-P. Hansen, *Phys. Rev. Lett.*, 1997, **79**, 3082–3085.
40 R. van Roij, M. Dijkstra and J.-P. Hansen, *Phys. Rev. E: Stat. Phys., Plasmas, Fluids, Relat. Interdiscip. Top.*, 1999, **59**, 2010–2025.
41 M. E. Leunissen, Ph.D. thesis, Utrecht University, The Netherlands, 2007, a digital copy can be obtained from www.colloid.nl.

42 M. T. Elsesser and A. D. Hollingsworth, *Langmuir*, 2010, **26**, 17989–17996.
43 G. Bosma, C. Pathmamanoharan, E. H. A. de Hoog, W. K. Kegel, A. van Blaaderen and H. N. W. Lekkerkerker, *J. Colloid Interface Sci.*, 2002, **245**, 292–300.
44 L. Antl, J. W. Goodwin, R. D. Hill, R. H. Ottewill, S. M. Owens, S. Papworth and J. A. Waters, *Colloids Surf.*, 1986, **17**, 67–78.
45 W. M. Heston, Jr, E. J. Hennelly and C. P. Smyth, *J. Am. Chem. Soc.*, 1950, **72**, 2071–2075.
46 T. Vissers, Ph.D. thesis, Utrecht University, The Netherlands, 2010, a digital copy can be obtained from www.colloid.nl.
47 E. J. W. Verwey and J. Th. G. Overbeek, *Theory of the stability of lyophobic colloids*, Elsevier, Amsterdam, 1948.
48 S. Alexander, P. M. Chaikin, P. Grant, G. J. Morales, P. Pincus and D. Hone, *J. Chem. Phys.*, 1984, **80**, 5776–5781.
49 M. E. Leunissen, C. G. Christova, A.-P. Hynninen, C. P. Royall, A. I. Campbell, A. Imhof, M. Dijkstra, R. van Roij and A. van Blaaderen, *Nature*, 2005, **437**, 235–240.
50 R. J. Hunter, *Zeta potential in colloid science. Principles and applications*, Academic Press, London, 1981.
51 J. C. Crocker and D. G. Grier, *J. Colloid Interface Sci.*, 1996, **179**, 298–310.
52 U. Dassanayake, S. Fraden and A. van Blaaderen, *J. Chem. Phys.*, 2000, **112**, 3851–3858.
53 R. J. Hunter, *Foundations of colloid science*, Oxford University Press, Oxford, 2nd edn, 2001.
54 P. J. Steinhardt, D. R. Nelson and M. Ronchetti, *Phys. Rev. B: Condens. Matter Mater. Phys.*, 1983, **28**, 784–805.
55 W. Lechner and C. Dellago, *J. Chem. Phys.*, 2008, **129**, 114707.
56 L. D. Landau and E. M. Lifshitz, *Quantum mechanics*, Pergamon, New York, 1965.
57 P. R. ten Wolde, M. J. Ruiz-Montero and D. Frenkel, *Phys. Rev. Lett.*, 1995, **75**, 2714–2717.
58 J. L. Finney, *Proc. R. Soc. London, Ser. A*, 1970, **319**, 479–493.
59 C. H. Bennett, *J. Appl. Phys.*, 1972, **43**, 2727–2734.
60 J. Jäckle, *Rep. Prog. Phys.*, 1986, **49**, 171–231.
61 S. P. Pan, J. Y. Qin, W. M. Wang and T. K. Gu, *Phys. Rev. B: Condens. Matter Mater. Phys.*, 2011, **84**, 092201.
62 D. E. Polk, *J. Non-Cryst. Solids*, 1973, **11**, 381–394.
63 E. J. Meijer and F. El Azhar, *J. Chem. Phys.*, 1997, **106**, 4678–4683.
64 F. El Azhar, M. Baus, J.-P. Ryckaert and E. J. Meijer, *J. Chem. Phys.*, 2000, **112**, 5121–5126.
65 A.-P. Hynninen and M. Dijkstra, *Phys. Rev. E: Stat., Nonlinear, Soft Matter Phys.*, 2003, **68**, 021407.
66 S. Auer and D. Frenkel, *J. Phys.: Condens. Matter*, 2002, **14**, 7667–7680.
67 N. A. M. Verhaegh, J. S. van Duijneveldt, A. van Blaaderen and H. N. W. Lekkerkerker, *J. Chem. Phys.*, 1995, **102**, 1416–1421.
68 J. P. Hoogenboom, D. Derks, P. Vergeer and A. van Blaaderen, *J. Chem. Phys.*, 2002, **117**, 11320–11328.
69 M. E. Leunissen and A. van Blaaderen, *J. Chem. Phys.*, 2008, **128**, 164509.
70 S. Hamaguchi, R. T. Farouki and D. H. E. Dubin, *Phys. Rev. E: Stat. Phys., Plasmas, Fluids, Relat. Interdiscip. Top.*, 1997, **56**, 4671–4682.
71 A.-P. Hynninen and M. Dijkstra, *Phys. Rev. Lett.*, 2005, **94**, 138303.
72 M. E. Leunissen, H. R. Vutukuri and A. van Blaaderen, *Adv. Mater.*, 2009, **21**, 3116–3120.
73 R. M. Erb, H. S. Son, B. Samanta, V. M. Rotello and B. B. Yellen, *Nature*, 2009, **457**, 999–1002.
74 M. N. van der Linden, A. van Blaaderen and M. Dijkstra, *J. Chem. Phys.*, 2013, **138**, 114903.